

Boundary Integral Methods for Particle Diffusion in Complex Geometries: Shielding, Confinement, and Escape

Jesse Cherry^a, Alan E. Lindsay^c, Bryan D. Quaipe^{a,b}

^a*Department of Scientific Computing, Florida State University, Tallahassee, FL, 32306.*

^b*Geophysical Fluid Dynamics Institute, Florida State University, Tallahassee, FL, 32306.*

^c*Department of Applied & Computational Math & Statistics, University of Notre Dame, Notre Dame, IN, 46656.*

Abstract

We present a numerical method for the solution of diffusion problems in unbounded planar regions with complex geometries of absorbing and reflecting bodies. Our numerical method applies the Laplace transform to the parabolic problem, yielding a modified Helmholtz equation which is solved with a boundary integral method. Returning to the time domain is achieved by quadrature of the inverse Laplace transform by deforming along the so-called Talbot contour. We demonstrate the method for various complex geometries formed by disjoint bodies of arbitrary shape on which either uniform Dirichlet or Neumann boundary conditions are applied. The use of the Laplace transform bypasses constraints with traditional time-stepping methods and allows for integration over the long equilibration timescales present in diffusion problems in unbounded domains. Using this method, we demonstrate shielding effects where the complex geometry modulates the dynamics of capture to absorbing sets. In particular, we show examples where geometry can guide diffusion processes to particular absorbing sites, obscure absorbing sites from diffusing particles, and even find the exits of confining geometries, such as mazes.

Keywords: Boundary Integral Equations, Diffusion Equation, Laplace Transform, First passage time problems.

1. Introduction

Many problems in biological transport involve a diffusing particle from a source to a fixed or mobile target [5, 6, 18, 40, 41, 46, 55]. The target, denoted by Γ_D , may be a preferred ecological habitat, a receptor on the surface of a cell, or an appropriate mate. Additionally, the particle may have to navigate through complex geometries and reflecting obstacles, denoted by Γ_N . In the scenario of unbiased diffusion in a planar region $\Omega \subset \mathbb{R}^2$, this requires solving the stochastic differential equation

$$d\mathbf{x} = \sqrt{2D} d\mathbf{W}, \quad t > 0, \quad \mathbf{x} \in \Omega; \quad \mathbf{x}(0) = \mathbf{x}^* \in \Omega. \quad (1a)$$

Here \mathbf{x}^* is the initial particle location, $D > 0$ is the diffusivity coefficient, and $d\mathbf{W}$ is the increment of a Weiner process. The main quantity of interest is the first arrival time τ at which the particle arrives at a target region Γ_D , given by

$$\tau = \min_{t>0} \{t \mid \mathbf{x}(t) \in \Gamma_D\}. \quad (1b)$$

Direct simulation of (1) offers a relatively straightforward method for sampling the distribution of τ , however, achieving high accuracy is tricky on account of errors near boundaries, the need to integrate for long times, and slow convergence of Monte Carlo methods. These issues can be mitigated with efficiency strategies such as Kinetic Monte Carlo [4, 39] or Walk on Spheres [24, 25, 48], however, it is desirable to have a deterministic solver for key quantities such as (1b).

In this work we propose to bypass these issues by solving directly for the density probability distribution of the particle. The forward Kolmogorov, or Fokker-Planck equation, describes the process (1) as a parabolic partial differential equation (PDE). We consider an unbounded multiply-connected domain $\Omega \subset \mathbb{R}^2$ with boundary $\Gamma = \partial\Omega$. For simplicity, we set the diffusivity to be $D = 1$ as shown in the schematic of Figure 1. The boundary condition on each component of Γ is homogeneous and can be either Dirichlet (absorbing bodies) or Neumann (reflecting bodies). The M_D components with Dirichlet boundary conditions are denoted by $\Gamma_D = \cup_{k=1}^{M_D} \Gamma_{D_k}$, and the M_N components with Neumann boundary conditions are denoted by $\Gamma_N = \cup_{k=1}^{M_N} \Gamma_{N_k}$. Therefore, $\Gamma = \Gamma_D \cup \Gamma_N$. Note that we do not allow for a single connected component of Γ to be divided into both Dirichlet and Neumann regions. Then, the governing equation is

$$\frac{\partial p}{\partial t} = \Delta p, \quad \mathbf{x} \in \Omega, \quad (2a)$$

$$p = 0, \quad \mathbf{x} \in \Gamma_D, \quad (2b)$$

$$\frac{\partial p}{\partial \mathbf{n}} = 0, \quad \mathbf{x} \in \Gamma_N, \quad (2c)$$

$$p(\mathbf{x}, 0) = \delta(\mathbf{x} - \mathbf{x}^*), \quad \mathbf{x} \in \Omega, \quad (2d)$$

where \mathbf{n} is the unit outward normal of Γ . The initial condition (2d) corresponds to the particle initially at $\mathbf{x}^* \in \Omega$. We also require that p is bounded as $|\mathbf{x}| \rightarrow \infty$.

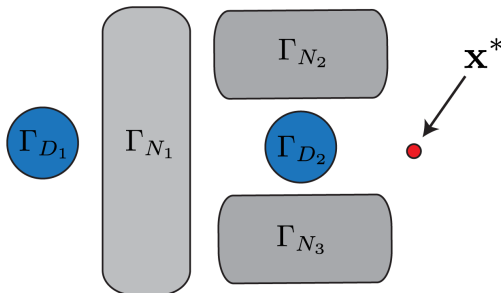


Figure 1: A schematic of the domain configuration comprising Neumann $\Gamma_N = \cup_{k=1}^{M_N} \Gamma_{N_k}$ and Dirichlet $\Gamma_D = \cup_{k=1}^{M_D} \Gamma_{D_k}$ components and source location $\mathbf{x}^* \in \Omega$.

A central quantity of interest from the solution of (2) is the flux through the target region, and its corresponding cumulative flux, defined as

$$j(t) = \int_{\Gamma_D} \frac{\partial p}{\partial \mathbf{n}} ds, \quad c(t) = \int_0^t j(\eta) d\eta, \quad (3)$$

respectively. The flux $j(t)$ gives the probability distribution of the first arrival time (1b) and typically has a large amount of mass at late time, so that the cumulative flux $c(t)$ converges to one

very slowly as $t \rightarrow \infty$. In terms of the capture time variable τ defined by (1), we have that

$$j(t) = \mathbb{P}(\tau = t), \quad c(t) = \mathbb{P}(\tau < t). \quad (4)$$

In this paper we develop a BIE method to solve the PDE (2), and to compute the flux $j(t)$ and cumulative flux $c(t)$ defined by (3). Integral equation methods offer a powerful technique over conventional stencil-based methods for solving PDEs, including: unbounded complex domains are easily incorporated, appropriately chosen formulations result in linear systems whose conditioning is mesh-independent, and linear complexity is possible by incorporating fast summation methods or fast direct solvers.

One approach to solve equation (2) is to first discretize the PDE in time, treating the diffusion term implicitly to reduce numerical stiffness. This results in an elliptic PDE that must be solved at each time step, and BIEs have been used to solve this PDE by many groups (Ex. [9, 16, 30]). A similar approach has been applied to other time-dependent PDEs such as the Navier-Stokes equations [1] and the wave equation [8]. Planar diffusion problems are characterized by long timescale dynamics, hence standard time stepping approaches are not practical as an excessively small time step size is required for temporal resolution.

Alternatively, the heat equation can be written in terms of the time-dependent heat kernel and this results in a Volterra integral equation. The regularity of the solution, and the compactness, and coercivity of the integral equations have been analyzed by several groups (Ex. [23, 29, 50]). A naive numerical approach to solve the integral equation requires storing and integrating over the entire time history, but this is computationally prohibitive. Greengard and Strain [20] introduced an optimal complexity algorithm that makes use of the smoothness of the history part of the heat kernel. A necessary algorithm of this approach is the Gauss transform, and this has led to several works on computing fast Gauss transforms [56, 62, 63]. Several groups perform a change of variables including a Fourier transform in space or time [19, 34], an Abel transform [43], a Chebyshev transform [14, 58, 61], or a Laplace transform of the heat kernel [26].

Rather than taking the Laplace transform of the heat kernel, we take the approach of using the Laplace transform to convert the time-dependent parabolic PDE to an parameter-based elliptic PDE. This requires a method to solve the resulting elliptic PDE, and to invert the Laplace transform [35]. Other groups have also combined BIEs with the Laplace transform and its inverse including for non-homogeneous heat conduction in bounded 2D and 3D domains [11, 54, 57].

A complementary approach to solving parabolic and elliptic PDEs, is to recast their solutions as probability distributions that can be sampled through Monte Carlo simulation of related diffusion problems [21, 25, 42, 49, 52]. Particle based methods can bypass obstacles inherent to stencil solution methods, for example resolving singularities at corners. However, they are slow to converge, relatively low accuracy, and prone to getting stuck near reflecting boundaries [12]. An additional advantage of the PDE approach developed here is that the density $p(\mathbf{x}, t)$ is obtained everywhere which yields much more detail on the trajectories of diffusing particles.

In this work, we combine a well-conditioned BIE formulation for the Laplace-transformed PDE, which involves both Dirichlet and Neumann boundary conditions, and then invert the Laplace transform with spectral accuracy by integrating along an appropriate contour in the complex plane. We demonstrate this method for the simulation of (2) in the presence of absorbing and reflecting obstacles as shown in the schematics Fig. 1.

The structure of the paper is as follows. In section 2, we detail our solution approach based on a combination of the Laplace transform with boundary integral equations. In section 3, we

describe numerical implementation details, in particular quadrature rules for the integrals and calculation of surface fluxes. In section 4, we provide a series of examples that both validate the expected convergence rate of the method and demonstrate its effectiveness on examples with complex geometries. In particular, our results demonstrate a *shielding* effect where capture statistics are modulated by geometric features. Finally in section 5 we conclude by highlighting avenues for future investigations.

2. Formulation

Consider the Laplace transform variable

$$P(\mathbf{x}, s) = \mathcal{L}[p](s) = \int_0^\infty e^{-st} p(\mathbf{x}, t) dt, \quad s \in \mathbb{C} \quad (5)$$

where a variable with a capital letter denotes the Laplace transform of the variable with the corresponding lower case letter. Taking the Laplace transform of (2), we obtain the elliptic PDE

$$(s - \Delta)P(\mathbf{x}, s) = \delta(\mathbf{x} - \mathbf{x}^*), \quad \mathbf{x} \in \Omega, \quad (6a)$$

$$P(\mathbf{x}, s) = 0, \quad \mathbf{x} \in \Gamma_D, \quad (6b)$$

$$\frac{\partial P}{\partial \mathbf{n}}(\mathbf{x}, s) = 0, \quad \mathbf{x} \in \Gamma_N. \quad (6c)$$

Note that the solution of this PDE depends on $s \in \mathbb{C}$. For a given s , we write P as

$$P(\mathbf{x}, s) = P^h(\mathbf{x}, s) + G(\mathbf{x} - \mathbf{x}^*), \quad (7)$$

where

$$G(\mathbf{x}) = \frac{1}{2\pi} K_0(\sqrt{s}|\mathbf{x}|), \quad (8)$$

is the fundamental solution of the differential operator $s - \Delta$. Note that the fundamental solution depends on the Laplace transform variable s . To satisfy boundary conditions, we require that $P^h(\mathbf{x}, s)$ satisfies

$$(s - \Delta)P^h = 0, \quad \mathbf{x} \in \Omega, \quad (9a)$$

$$P^h(\mathbf{x}, s) = -G(\mathbf{x} - \mathbf{x}^*), \quad \mathbf{x} \in \Gamma_D, \quad (9b)$$

$$\frac{\partial P^h}{\partial \mathbf{n}}(\mathbf{x}, s) = -\frac{\partial G}{\partial \mathbf{n}}(\mathbf{x} - \mathbf{x}^*), \quad \mathbf{x} \in \Gamma_N. \quad (9c)$$

Having a method to solve equation (6), we compute $p(\mathbf{x}, t)$ by applying the inverse Laplace transform as described in Section 2.3. We note that since the PDE is linear, our method can be generalized to the case where the initial condition is a finite sum of weighted delta functions centered at different points in Ω . In the following sections we describe integral equation methods to solve both the homogeneous PDE (9) and to calculate the Bromwich integral that inverts the Laplace transform.

2.1. Boundary Integral Equation Formulation

We solve the mixed boundary condition elliptic PDE (9) using a BIE method. In this manner, we are able to resolve complex geometries, achieve high-order accuracy, and satisfy the far-field boundary condition. We account for the mixed boundary conditions by choosing a layer potential formulation that results in a well-conditioned system of integral equations. In particular, we express $P^h(\mathbf{x}, s)$ as a sum of double- and single-layer potentials

$$P^h(\mathbf{x}, s) = \mathcal{D}[\sigma_D](\mathbf{x}) + \mathcal{S}[\sigma_N](\mathbf{x}), \quad (10)$$

where

$$\mathcal{D}[\sigma_D](\mathbf{x}) = \frac{1}{2\pi} \int_{\Gamma_D} \frac{\partial}{\partial \mathbf{n}_y} G(\mathbf{x} - \mathbf{y}) \sigma_D(\mathbf{y}) ds_y, \quad (11)$$

$$\mathcal{S}[\sigma_N](\mathbf{x}) = \frac{1}{2\pi} \int_{\Gamma_N} G(\mathbf{x} - \mathbf{y}) \sigma_N(\mathbf{y}) ds_y, \quad (12)$$

and G is defined in (8). We use the unknown density functions σ_N and σ_D to satisfy the boundary conditions by matching the limiting value of $P^h(\mathbf{x}, s)$ as \mathbf{x} approaches Γ_N and Γ_D with the appropriate boundary condition. In particular, the density functions satisfy the system of second-kind Fredholm integral equations

$$-G(\mathbf{x} - \mathbf{x}^*) = +\frac{1}{2}\sigma_D(\mathbf{x}) + \mathcal{D}[\sigma_D](\mathbf{x}) + \mathcal{S}[\sigma_N](\mathbf{x}), \quad \mathbf{x} \in \Gamma_D, \quad (13a)$$

$$-\frac{\partial}{\partial \mathbf{n}} G(\mathbf{x} - \mathbf{x}^*) = -\frac{1}{2}\sigma_N(\mathbf{x}) + \frac{\partial}{\partial \mathbf{n}} \mathcal{D}[\sigma_D](\mathbf{x}) + \frac{\partial}{\partial \mathbf{n}} \mathcal{S}[\sigma_N](\mathbf{x}), \quad \mathbf{x} \in \Gamma_N, \quad (13b)$$

where the normal derivatives are taken at the target point \mathbf{x} . The system of integral equations can be written in matrix form as

$$-\begin{bmatrix} G \\ \partial_{\mathbf{n}} G \end{bmatrix} = \begin{bmatrix} \frac{1}{2} & 0 \\ 0 & -\frac{1}{2} \end{bmatrix} \begin{bmatrix} \sigma_D \\ \sigma_N \end{bmatrix} + \begin{bmatrix} \mathcal{D} & \mathcal{S} \\ \partial_{\mathbf{n}} \mathcal{D} & \partial_{\mathbf{n}} \mathcal{S} \end{bmatrix} \begin{bmatrix} \sigma_D \\ \sigma_N \end{bmatrix}, \quad (14)$$

where we have dropped the independent variable. Note that the diagonal terms of the diagonal blocks are continuous (see Section 3.1), and the off-diagonal blocks are continuous since the target and source points are on different connected components of Γ . Therefore, all the integral operators in (13) are compact.

2.2. Computing the Flux Through Γ_D

To compute the flux $j(t)$, as defined in equation (3), we first take the normal derivative and integrate the Laplace transform of p . That is, we compute the flux of equation (7), where P^h is a sum of layer potentials (10). In particular, we compute

$$J(s) = \int_{\Gamma_D} \frac{\partial}{\partial \mathbf{n}} P(\mathbf{x}, s) ds_{\mathbf{x}} = \int_{\Gamma_D} \frac{\partial}{\partial \mathbf{n}} \left(P^h(\mathbf{x}, s) + G(\mathbf{x} - \mathbf{x}^*) \right) ds_{\mathbf{x}}. \quad (15)$$

We also compute the Laplace transform of the cumulative flux of j , which by properties of the Laplace transform is $C(s) = s^{-1}J(s)$. Finally, the flux and the cumulative flux are computed in the time variable by taking an inverse Laplace transform as described in Section 2.3.

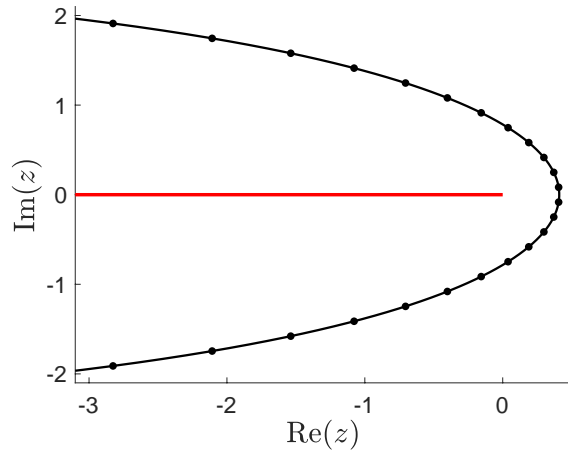


Figure 2: The Talbot (solid black) contour (18). Integration along the Talbot contour is done with the midpoint rule, and the black marks are the resulting quadrature points with $M = 24$. The singularities of $P(\mathbf{x}, s)$ are along the negative real axis (solid red).

2.3. Inverting the Laplace Transform

The inverse Laplace transform, also known as the Bromwich integral, is

$$\mathcal{L}^{-1}[P](\mathbf{x}, s) = \frac{1}{2\pi i} \int_B e^{st} P(\mathbf{x}, s) ds, \quad \mathbf{x} \in \Omega, \quad (16)$$

where

$$B = \{\alpha + is \mid s \in \mathbb{R}\}, \quad (17)$$

and α is greater than the real part of all the poles of $P(\mathbf{x}, s)$. The contour B is called the Bromwich contour. The poles of P all lie on the negative real axis, so we can choose any value $\alpha > 0$. Along the Bromwich contour B , the integrand $e^{st}P(\mathbf{x}, s)$ decays algebraically and oscillates wildly, especially for large t . Therefore, an unpractical number of quadrature points is required to numerically compute the Bromwich integral.

Alternatively, we can replace the contour B with any other contour, so long as all the poles of $P(\mathbf{x}, s)$ remain on the same side of this new contour. There are a variety of choices [59], and we opt to use the Talbot contour,

$$T = \left\{ \frac{2M}{t} (-0.6122 + 0.5017\theta \cot(0.6407\theta) + 0.2645i\theta) \mid \theta \in (-\pi, \pi) \right\}, \quad (18)$$

which was first introduced by Dingfelder and Weideman [15]. The contour depends on both the time t and the number of quadrature points $2M$. We use $2M$ total quadrature points on the Talbot contour because we are working with real-valued functions in the time domain, and the integral can be computed along points on the Talbot contour with $\theta \geq 0$, and then doubling the result. Although the Talbot contour T does not extend to infinity, the magnitude of the integrand at $\theta = \pm\pi$ is less than machine epsilon, so the error introduced by integrating along T rather than B is numerically zero. In contrast to the Bromwich contour, the integrand $e^{st}P(s, t)$ is smooth and does not oscillate along the Talbot contour T . The contour is illustrated in Figure 2 (black curve), and the poles of $P(\mathbf{x}, s)$ are all located along the red line. The black points are quadrature points that are described in Section 3.3.

3. Numerical Methods

Section 2 introduced several integrals that need to be evaluated in order to solve the heat equation (2) and the corresponding flux (3). This section describes the quadrature techniques we use to solve the second-kind Fredholm integral equation (13) and to evaluate the double-layer potential (10) (Section 3.1), to compute the flux through Γ_D (Section 3.2), and to compute the Talbot integral (Section 3.3).

3.1. Solving the BIE

We assume that there are M_D components of Γ_D and M_N components of Γ_N . Each component is parameterized as $\mathbf{y}^k(\alpha)$, where $k = 1, \dots, M_D + M_N$ and $\alpha \in [0, 2\pi)$. The first M_D components are the Dirichlet components, and the other M_N components are the Neumann components. Then, the system of BIEs (13) are discretized with a collocation method by discretizing $[0, 2\pi)$ at N equispaced points. We approximate the integrals with the trapezoid rule, resulting in the linear system

$$f_n^k = \frac{1}{2}\sigma_n^k + \frac{2\pi}{N} \sum_{m=1}^{M_D} \sum_{\ell=1}^N \frac{\partial}{\partial \mathbf{n}_\ell^m} G(\mathbf{y}_n^k - \mathbf{y}_\ell^m) \sigma_\ell^m + \frac{2\pi}{N} \sum_{m=M_D+1}^{M_D+M_N} \sum_{\ell=1}^N G(\mathbf{y}_n^k - \mathbf{y}_\ell^m) \sigma_\ell^m, \\ k = 1, \dots, M_D, n = 1, \dots, N \quad (19a)$$

$$g_n^k = -\frac{1}{2}\sigma_n^k + \frac{2\pi}{N} \sum_{m=1}^{M_D} \sum_{\ell=1}^N \frac{\partial}{\partial \mathbf{n}_n^k} \frac{\partial}{\partial \mathbf{n}_\ell^m} G(\mathbf{y}_n^k - \mathbf{y}_\ell^m) \sigma_\ell^m + \frac{2\pi}{N} \sum_{m=M_D+1}^{M_D+M_N} \sum_{\ell=1}^N \frac{\partial}{\partial \mathbf{n}_n^k} G(\mathbf{y}_n^k - \mathbf{y}_\ell^m) \sigma_\ell^m, \\ k = M_D + 1, \dots, M_D + M_N, n = 1, \dots, N, \quad (19b)$$

where

$$\sigma_\ell^m = \sigma(\mathbf{y}^m(\alpha_\ell)) \left| \frac{\partial}{\partial \alpha} \mathbf{y}^m(\alpha_\ell) \right|, \quad (20)$$

and the left-hand sides are

$$f_n^k = -G(\mathbf{y}_n^k - \mathbf{y}^*), \text{ and } g_n^k = -\frac{\partial}{\partial \mathbf{n}_n^k} G(\mathbf{y}_n^k - \mathbf{y}^*). \quad (21)$$

Our notation uses a superscript to denote the body being considered, and the subscript denotes the discretization point on that particular body. Since the superscript determines if the density function is defined on a Neumann or Dirichlet body, we do not need to specify whether the discretized version of corresponds to σ_D or σ_N .

Because the fundamental solution involves the modified Bessel function of the second kind, the second summand in equation (19a) has a logarithmic singularity when $\ell = n$ and $m = k$. However, this never occurs since k and m never coincide. For the same reason, the first summand in equation (19b) has no singularities. However, the first summand of equation (19a), and the second summand of equation (19b) cannot be naively evaluated when $\ell = n$ and $m = k$, but the singularities of the kernels are removable. Therefore, the terms in the summation when $\ell = n$ and $m = k$ are replaced with their limiting values

$$\lim_{\substack{\mathbf{y} \rightarrow \mathbf{x} \\ \mathbf{x} \in \Gamma}} \frac{\partial}{\partial \mathbf{n}_\mathbf{y}} G(\mathbf{x} - \mathbf{y}) = -\frac{1}{2}\kappa(\mathbf{x}), \quad \lim_{\substack{\mathbf{y} \rightarrow \mathbf{x} \\ \mathbf{x} \in \Gamma}} \frac{\partial}{\partial \mathbf{n}_\mathbf{x}} G(\mathbf{x} - \mathbf{y}) = +\frac{1}{2}\kappa(\mathbf{x}), \quad (22)$$

where $\kappa(\mathbf{x})$ is the curvature at the surface point $\mathbf{x} \in \Gamma$.

A numerical issue with BIE solvers is near-singular integration which occurs when two different components of Γ are close to one another. Independent of the value of N , the error of the trapezoid rule will grow without bound. There are a suite of quadrature methods that address nearly-singular integrals, but these are not the focus of this work. Instead, we use geometries whose components are sufficiently separated that the problems can achieve sufficient accuracy for values of N that can be implemented on a standard laptop. The smoothness of the kernels, particularly the regularity of the kernels of the double-layer potential and normal derivative of the single-layer potential, determines the convergence with respect to N . Since these kernels are both normal derivatives of the modified Bessel function, the kernel is C^1 , and therefore the trapezoid rule achieves third-order accuracy [31]. This spatial convergence behavior is demonstrated in Section 4.2. We note that higher-order accuracy is possible using a variety of quadrature methods [2, 22, 27].

Since we are solving a second-kind Fredholm integral equation, and all the kernels are continuous, the discretization (19) can be solved with a mesh-independent number of GMRES iterations [7]. Therefore, the computational cost of solving (19) is proportional to the cost of computing the necessary summations at all target points. We use a direct calculation to compute these sums, therefore requiring $\mathcal{O}((M_D + M_N)^2 N^2)$ operations. In future work, we will use a direct solver or a fast summation method to reduce the computational cost.

3.2. Computing the Flux

The Laplace transform of the flux into the absorbing bodies is given by equation (15). We must compute the normal derivative, followed by a boundary integral around Γ_D , of two terms: the Green's function centered at \mathbf{x}^* , and the layer potential representation of $P^h(\mathbf{x}, s)$. The former of these two terms is computed exactly by calculating the normal derivative of equation (8), and since $\mathbf{x}^* \notin \Gamma_D$, the integral is computed with spectral accuracy with the trapezoid rule. However, the latter term requires quadrature to compute

$$\begin{aligned} \int_{\Gamma_D} \frac{\partial}{\partial \mathbf{n}} P^h(\mathbf{x}, s) ds_{\mathbf{x}} &= \int_{\Gamma_D} \frac{\partial}{\partial \mathbf{n}} (\mathcal{D}[\sigma_D](\mathbf{x}) + \mathcal{S}[\sigma_N](\mathbf{x})) ds_{\mathbf{x}} \\ &= \int_{\Gamma_D} \frac{\partial}{\partial \mathbf{n}} \left(\int_{\Gamma_D} \frac{\partial}{\partial \mathbf{n}_{\mathbf{y}}} G(\mathbf{x} - \mathbf{y}) \sigma_D(\mathbf{y}) ds_{\mathbf{y}} + \int_{\Gamma_N} G(\mathbf{x} - \mathbf{y}) \sigma_N(\mathbf{y}) ds_{\mathbf{y}} \right) ds_{\mathbf{x}} \\ &= \int_{\Gamma_D} \int_{\Gamma_D} \frac{\partial^2}{\partial \mathbf{n} \partial \mathbf{n}_{\mathbf{y}}} G(\mathbf{x} - \mathbf{y}) \sigma_D(\mathbf{y}) ds_{\mathbf{y}} ds_{\mathbf{x}} + \int_{\Gamma_D} \int_{\Gamma_N} \frac{\partial}{\partial \mathbf{n}} G(\mathbf{x} - \mathbf{y}) \sigma_N(\mathbf{y}) ds_{\mathbf{y}} ds_{\mathbf{x}}. \end{aligned} \quad (23)$$

Since $\mathbf{x} \in \Gamma_D$ and $\mathbf{y} \in \Gamma_N$, and these two contours do not intersect, we accurately compute the second integral in equation (23) with the trapezoid rule. That is

$$\int_{\Gamma_D} \int_{\Gamma_N} \frac{\partial}{\partial \mathbf{n}} G(\mathbf{x} - \mathbf{y}) \sigma_N(\mathbf{y}) ds_{\mathbf{y}} ds_{\mathbf{x}} \approx \left(\frac{2\pi}{N} \right)^2 \sum_{k=1}^{M_D} \sum_{n=1}^N \sum_{m=M_D+1}^{M_D+M_N} \sum_{\ell=1}^N \frac{\partial}{\partial \mathbf{n}_n^k} G(\mathbf{y}_n^k - \mathbf{y}_\ell^m) \sigma_\ell^m. \quad (24)$$

The first integral in equation (23) requires more care since $\mathbf{x} \in \Gamma_D$ and $\mathbf{y} \in \Gamma_D$, and the singularity of the kernel scales as $|\mathbf{x} - \mathbf{y}|^{-2}$ as $\mathbf{x} \rightarrow \mathbf{y}$. Therefore, the trapezoid rule will not converge to the principal value integral. Instead, the integral is manipulated with a careful use of singularity

subtraction [47]

$$\begin{aligned}
\int_{\Gamma_D} \int_{\Gamma_D} \frac{\partial^2}{\partial \mathbf{n} \partial \mathbf{n}_y} G(\mathbf{x} - \mathbf{y}) \sigma_D(\mathbf{y}) ds_y ds_x &= \frac{1}{2\pi} \int_{\Gamma_D} \int_{\Gamma_D} \frac{\partial^2}{\partial \mathbf{n} \partial \mathbf{n}_y} K_0(\sqrt{s}|\mathbf{x} - \mathbf{y}|) \sigma_D(\mathbf{y}) ds_y ds_x \\
&= \frac{1}{2\pi} \int_{\Gamma_D} \int_{\Gamma_D} \frac{\partial^2}{\partial \mathbf{n} \partial \mathbf{n}_y} (K_0(\sqrt{s}|\mathbf{x} - \mathbf{y}|) + \log|\mathbf{x} - \mathbf{y}|) \sigma_D(\mathbf{y}) ds_y ds_x \\
&\quad - \frac{1}{2\pi} \int_{\Gamma_D} \int_{\Gamma_D} \frac{\partial^2}{\partial \mathbf{n} \partial \mathbf{n}_y} \log|\mathbf{x} - \mathbf{y}| \sigma_D(\mathbf{y}) ds_y ds_x.
\end{aligned} \tag{25}$$

Equation (25) simply introduces the addition and subtraction of a term. The particular choice guarantees that the two integrals can be individually computed accurately or analytically. Based on the asymptotics of the modified Bessel function, the singularity of the first integrand scales with $|\mathbf{x} - \mathbf{y}|^{-1}$ as $\mathbf{x} \rightarrow \mathbf{y}$, and the integrand is computed using odd-even integration [53]. The error of this quadrature method is first-order accurate, but, as mentioned earlier, higher-order accuracy is possible by using other more expensive quadrature rules. The second integral is identically zero since

$$\begin{aligned}
\frac{1}{2\pi} \int_{\Gamma_D} \int_{\Gamma_D} \frac{\partial^2}{\partial \mathbf{n} \partial \mathbf{n}_y} \log|\mathbf{x} - \mathbf{y}| \sigma_D(\mathbf{y}) ds_y ds_x &= \frac{1}{2\pi} \int_{\Gamma_D} \frac{\partial}{\partial \mathbf{n}} \int_{\Gamma_D} \frac{\partial}{\partial \mathbf{n}_y} \log|\mathbf{x} - \mathbf{y}| \sigma_D(\mathbf{y}) ds_y ds_x \\
&= \frac{1}{2\pi} \int_{\Omega} \Delta \left(\int_{\Gamma_D} \frac{\partial}{\partial \mathbf{n}_y} \log|\mathbf{x} - \mathbf{y}| \sigma_D(\mathbf{y}) ds_y \right) d\mathbf{x} = 0,
\end{aligned} \tag{26}$$

where the inner integral is zero because the integrand is the double-layer potential of Laplace's equation.

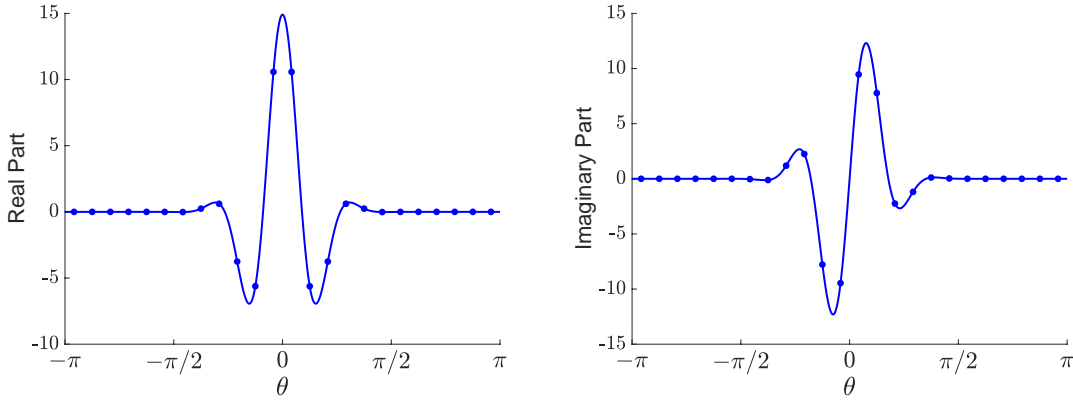


Figure 3: The real and imaginary parts of a typical integrand required to compute a Talbot integral. The truncation of the integrand and the choice of the Talbot contour guarantee that the quadrature error is $\mathcal{O}(10^{-1.2M})$, until M is sufficiently large that machine precision is reached.

3.3. Computing the Inverse Laplace Transform

Figure 2 illustrates the Talbot contour we use, which, to the best of our knowledge, achieves the highest-order accuracy known to date. Spectral accuracy is achieved by applying the midpoint rule, and the midpoint quadrature points are the black points in Figure 2. The integrand for an example from Section 4.1 is shown in Figure 3. The marks indicate the quadrature points used for

the trapezoid rule with $M = 12$ and $t = 10$. The magnitude of the integrand at the final quadrature points is on the order of 10^{-14} , so truncation errors can be safely ignored.

The lack of oscillatory behavior and the decay rate of the integrand guarantee that the midpoint rule achieves spectral accuracy with an error that scales as $10^{-1.2M}$. In Section 4.1, we demonstrate this temporal order of convergence by applying the quadrature to the Laplace transform of the one-dimensional heat equation.

As noted by Dingfeld and Weideman [15], floating-point error dominates the midpoint rule if M is too large. They control this error by adjusting the Talbot contour when necessary. We take this same approach for the one-dimensional heat equation in Section 4.1, and observe that this adjustment should be made when $M > 12$. Therefore, to compute the inverse Laplace transform for all other numerical examples, we apply the midpoint rule to equation (18) with $M = 12$ quadrature points.

4. Numerical Results

In this section, we demonstrate the accuracy and utility of the formulation and numerical methods described in Sections 2 and 3. We first demonstrate that the expected orders of accuracy are achieved in time (Section 4.1) and in space (Section 4.2). Then, we consider several complex geometries to demonstrate the effect of screening the absorbing body with a collection of absorbing and reflecting bodies (Sections 4.3–4.5).

4.1. Talbot Integral Convergence

We first demonstrate that the method achieves the expected rate of convergence in time by considering the exactly solvable one-dimensional heat equation in the interval $x \in [-\pi, \pi]$. Specifically, we solve

$$\frac{\partial p}{\partial t} = \frac{\partial^2 p}{\partial x^2}, \quad x \in (-\pi, \pi), \quad t > 0, \quad (27a)$$

$$p(-\pi, t) = p(\pi, t) = 0, \quad t > 0, \quad (27b)$$

$$p(x, 0) = \delta(x), \quad x \in (-\pi, \pi). \quad (27c)$$

The Laplace transform $P(x, s) = \mathcal{L}[p](s) = \int_0^\infty e^{-st} p(x, t) dt$ solves the modified Helmholtz problem

$$sP - \frac{\partial^2 P}{\partial x^2} = \delta(x), \quad x \in (-\pi, \pi), \quad s \in \mathbb{C}, \quad (28a)$$

$$P(-\pi, s) = P(\pi, s) = 0, \quad (28b)$$

whose exact solution is

$$P(x, s) = \frac{\sinh[\sqrt{s}(\pi - |x|)]}{2\sqrt{s} \cosh \sqrt{s}\pi}. \quad (29)$$

Therefore the solution $p(x, t)$ can be expressed with the inverse Laplace transform

$$p(x, t) = \frac{1}{2\pi i} \int_B e^{st} P(x, s) ds = \frac{1}{2\pi i} \int_B e^{st} \frac{\sinh[\sqrt{s}(\pi - |x|)]}{2\sqrt{s} \cosh \sqrt{s}\pi} ds, \quad (30)$$

where B is the Bromwich contour. Applying the transformation $s = z^2$ yields

$$p(x, t) = \frac{1}{2\pi i} \int_{B'} f(z) dz, \quad f(z) = e^{z^2 t} \frac{\sinh[z(\pi - |x|)]}{\cosh z\pi}, \quad (31)$$

where B' is the transformed Bromwich contour, and this integral can be evaluated with standard residue calculus. In particular, the integrand of (31) has simple poles $z = i(n - \frac{1}{2})$ for $n = 1, 2, 3, \dots$. To apply the residue theorem, we identify that

$$\text{Res}(f(z), i(n - \frac{1}{2})) = \frac{1}{\pi} e^{-(n - \frac{1}{2})^2 t} \cos[(n - \frac{1}{2})x]. \quad (32)$$

Hence we arrive at the solution of (27)

$$p_{\text{ex}}(x, t) = 2\pi i \frac{1}{2\pi i} \sum_{n=1}^{\infty} \text{Res}(f(z), i(n - \frac{1}{2})) = \frac{1}{\pi} \sum_{n=1}^{\infty} e^{-(n - \frac{1}{2})^2 t} \cos[(n - \frac{1}{2})x], \quad (33)$$

which coincides with the solution derived by separation of variables. We now evaluate the error of the numerical inverse procedure applied to (30) by comparing with the series solution (33). In particular, the inverse Laplace transform is computed by applying the M -point midpoint rule along the Talbot contour T defined in equation (18). As the number of quadrature points increases, round-off error associated with evaluation of e^{st} becomes sizable. We implement a round-off control algorithm [15, Sec. 3] to prevent this issue from introducing large errors. For a selection of times, Figure 4 shows the exact solution, the numerical solution, and the error

$$\mathcal{E}_{\text{inf}} = \max_{x \in (-\pi, \pi)} |p(x, t) - p_{\text{ex}}(x, t)|, \quad (34)$$

for different number M of Talbot quadrature points. The expected exponential order of convergence is achieved until the error reaches machine precision.

4.2. Boundary Integral Equation Convergence

Having validated the convergence of the Talbot integration, we examine the convergence behavior of the BIE solver by considering a two-dimensional problem with a closed form solution. We let $\Omega = \mathbb{R}^2 \setminus B(0, 1)$ where $B(0, 1)$ is the unit ball centered at the origin, and impose a homogeneous Dirichlet boundary condition on $\partial\Omega$. The initial condition is the delta function centered at $\mathbf{x}^* = (x_0, 0)$, for $x_0 > 1$.

The governing equation for $P = P(r, \theta; s)$ in polar coordinates $\mathbf{x} = r(\cos \theta, \sin \theta)$ with $R = |\mathbf{x}^*|$ is

$$\frac{\partial^2 P}{\partial r^2} + \frac{1}{r} \frac{\partial P}{\partial r} + \frac{1}{r^2} \frac{\partial^2 P}{\partial \theta^2} - sP = -\frac{1}{r} \delta(r - R) \delta(\theta), \quad r > 1, \quad \theta \in (-\pi, \pi), \quad s \in \mathbb{C}, \quad (35a)$$

$$P(r, \theta + 2\pi) = P(r, \theta), \quad r > 1, \quad (35b)$$

$$P(1, \theta) = 0, \quad \theta \in (-\pi, \pi). \quad (35c)$$

The exact solution of P is the Fourier cosine series [55, equation (A5)]

$$P(r, \theta; s) = \begin{cases} \sum_{n=0}^{\infty} A_n \left[I_n(\sqrt{s}r) - \frac{I_n(\sqrt{s})}{K_n(\sqrt{s})} K_n(\sqrt{s}r) \right] \cos n\theta, & r \in (1, R], \\ \sum_{n=0}^{\infty} A_n \left[\frac{I_n(\sqrt{s}R)}{K_n(\sqrt{s}R)} - \frac{I_n(\sqrt{s})}{K_n(\sqrt{s})} \right] K_n(\sqrt{s}r) \cos n\theta, & r \in (R, \infty), \end{cases} \quad (36a)$$

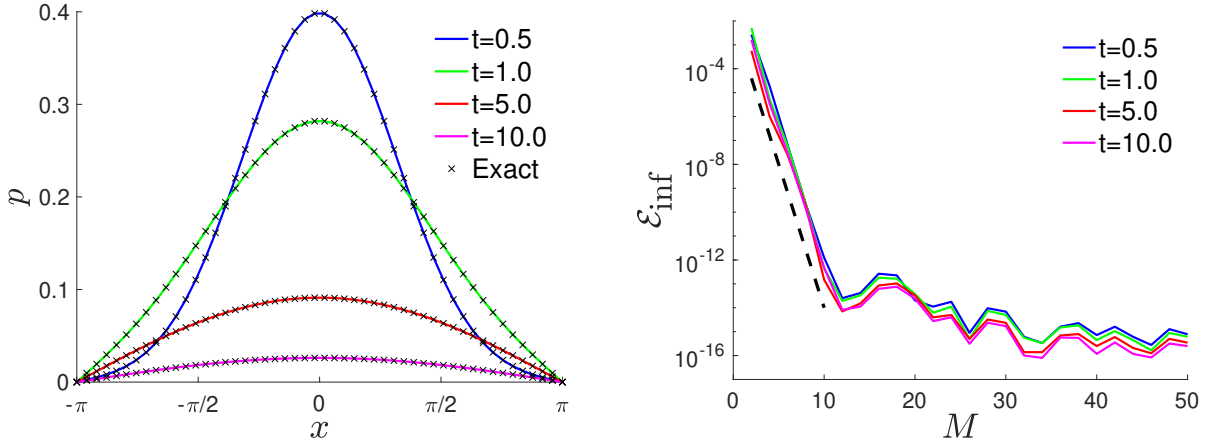


Figure 4: A verification of the convergence of Talbot integration on the exactly solvable 1D heat equation (27). The left plot shows the exact and approximate solutions, and the right plot shows the error at four different times as a function of the number of Talbot quadrature points. For $M \leq 12$, the error converges as $10^{-1.2M}$ (black dashed curve). If the same Talbot contour were used for larger values of M , round-off error would begin to dominate the quadrature error. Therefore, for these larger values of M , the Talbot contour is slightly modified [15].

where the constants A_n are

$$A_n = \begin{cases} \frac{1}{2\pi} K_0(\sqrt{s}R), & n = 0, \\ \frac{1}{\pi} K_n(\sqrt{s}R), & n \geq 1. \end{cases} \quad (36b)$$

The series solution (36) suffers from overflow and underflow error when $|\mathbf{x}|$ and $|\mathbf{x}^*|$ are too close, and this is demonstrated in Figure 5. In particular, we consider four different locations \mathbf{x} where the error of the numerical solution is computed for increasing values of N . If $|\mathbf{x}|$ is sufficiently smaller or larger than $|\mathbf{x}^*|$, then the expected third-order convergence is observed for different values of s . However, when $|\mathbf{x}|$ and $|\mathbf{x}^*|$ are too close (gray region), underflow results in an incorrect exact solution, and ultimately results in the error plateauing above machine precision as N increases.

In addition, we can calculate a series solution for the Laplace transform of the flux,

$$J(s) = \int_{\Gamma_D} P_r|_{r=1} ds = \frac{K_0(\sqrt{s}R)}{K_0(\sqrt{s})}. \quad (37)$$

Since the Laplace transform of the cumulative flux satisfies $sC(s) = J(s)$, we obtain the series solution for $C(s)$,

$$C(s) = \frac{J(s)}{s} = \frac{K_0(\sqrt{s}R)}{sK_0(\sqrt{s})}. \quad (38)$$

4.3. Navigating a Complex Geometry

We consider a particle navigating to a single absorbing body in the middle of a single *spiral-shaped* reflecting body (Figure 6). The absorbing body is a unit circle centered at the origin, and we solve the governing equations with two different sources: $\mathbf{x}^* = (8, 0)$ is near the opening of the

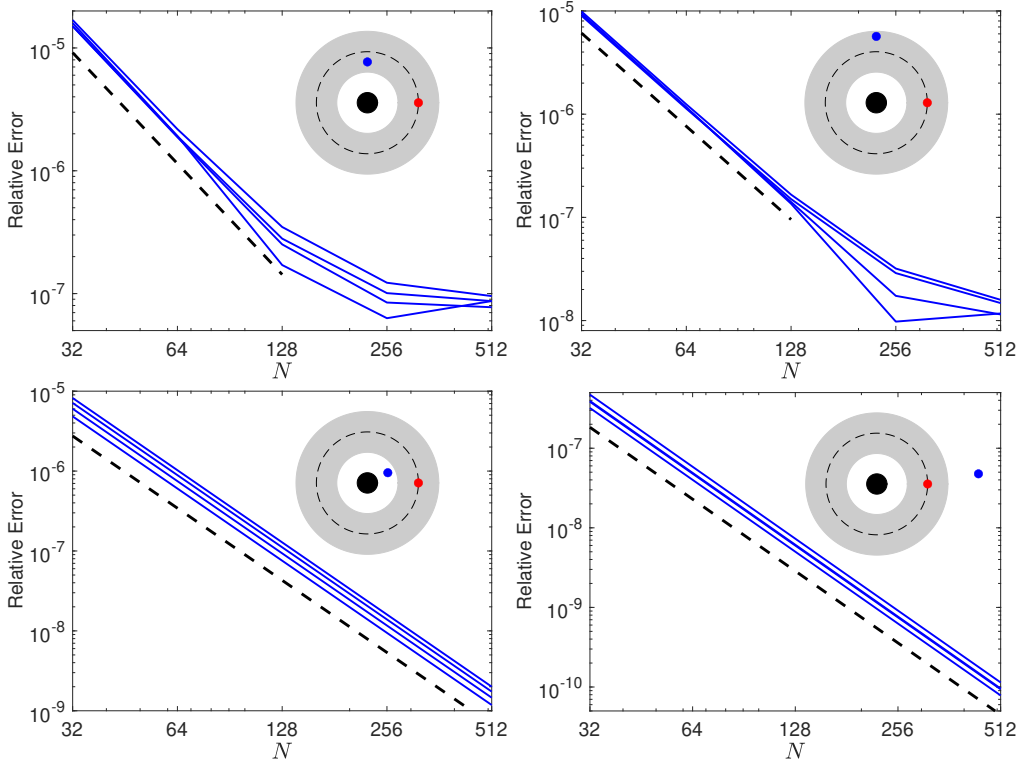


Figure 5: A spatial convergence study of the BIE solver at four target points for increasing number of collocation points N . The black circle in the middle of the inset is the absorbing body. Each blue curve represents a particular s -value on the Talbot contour at time $t = 10$. The dashed black lines indicate third-order convergence. If the modulus of the target (blue point) is too close (gray region) to the modulus of the initial particle location (red point), then the exact solution has round-off error which results in the loss of convergence for large N .

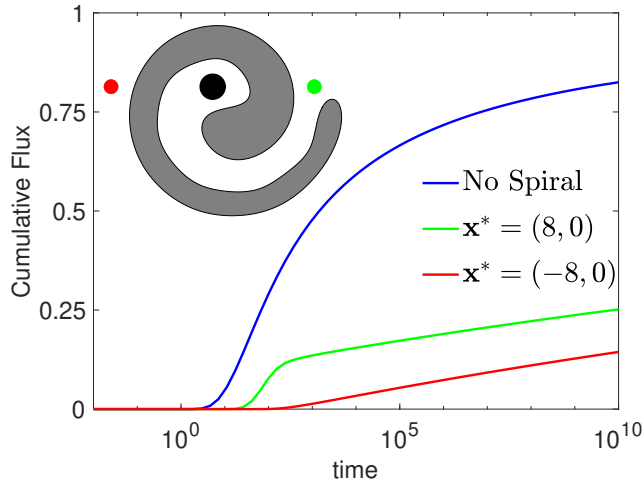


Figure 6: Three cumulative flux into the absorbing trap (black circle) in the middle of a reflecting spiral (gray body). Two experiments are initiated by particles at $\mathbf{x}^* = (-8, 0)$ (red) and $\mathbf{x}^* = (8, 0)$ (green). The blue curve displays the cumulative flux in the absence of the spiral and hence the capture rate in the absence of geometric effects.

spiral (green mark), and $\mathbf{x}^* = (-8, 0)$ is at the back of the spiral (red mark). Since the initial particle location of the latter example is farther from the opening of the spiral, we expect later arrival times into the absorbing body. As expected, the cumulative flux remains nearly zero for a very long time, then slowly starts to increase around $t = 10^2$. With the spiral reflecting body, the probability of capture by $t = 10^{10}$ from $\mathbf{x}^* = (8, 0)$ is only 25% while from $\mathbf{x}^* = (-8, 0)$, the equivalent probability is only 15%. As a baseline, we include the cumulative flux when the reflecting spiral is absent (blue curve).

A heat map of $p(\mathbf{x}, t)$ is shown in Figure 7 for both initial locations, and at three values of t . Consistent with the cumulative flux, we observe that a particle initiated near the opening of the spiral is much more likely to be found near the absorbing body when compared to a particle initiated at the location opposite the spiral opening. Hence, this demonstrates a simple geometric scenario where the capture rate is highly modulated by geometric features.

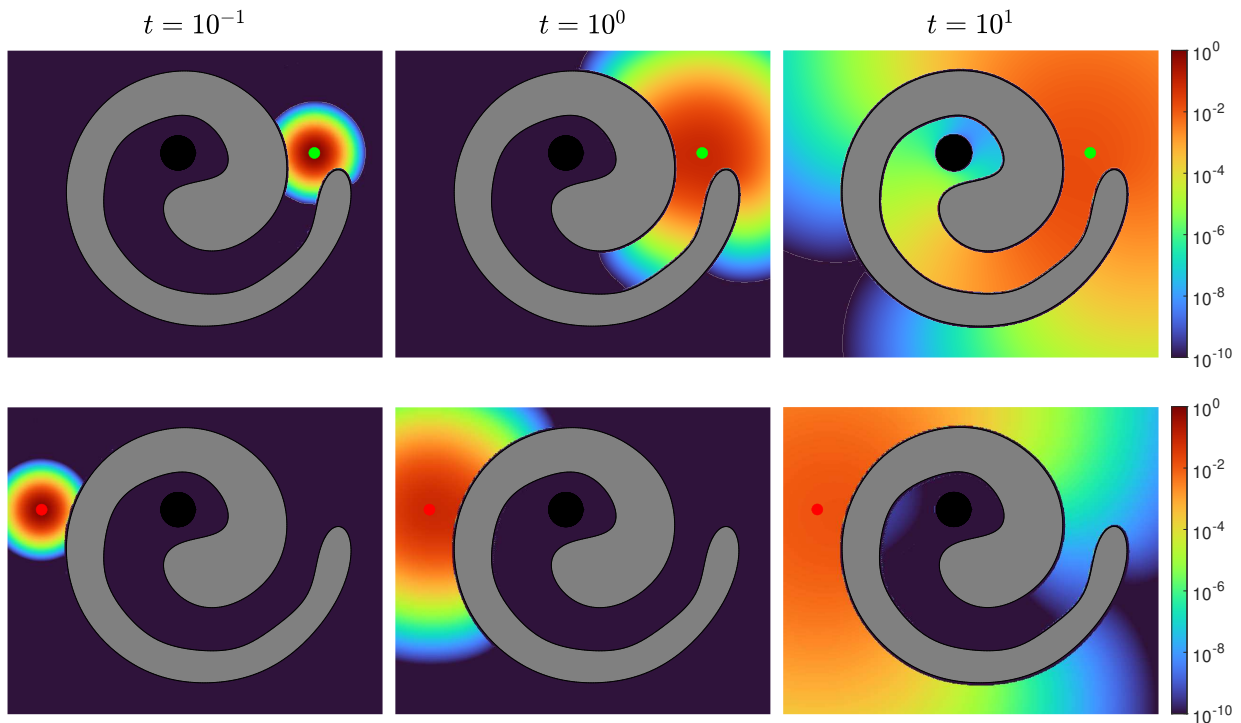


Figure 7: A heat map of solutions $p(\mathbf{x}, t)$ of (2) at three times $t = \{10^{-1}, 10^0, 10^1\}$. The gray spiral is reflecting, the black disk is absorbing, and the particle is initialized at the green dot (top row) and red dot (bottom row).

4.4. Shielding Effects in the Faraday Cage

Inspired by the Faraday cage, which blocks electromagnetic fields from an enclosure [10], we investigate the effect of shielding a Brownian particle by placing eight reflecting bodies around an absorbing body. The absorbing body is a unit circle centered at the origin, and the particle source is initially positioned at $\mathbf{x}^* = (5, 0)$. The centers of the reflecting bodies are evenly distributed at the eight roots of unity on a circle of radius three. We increase the shielding effect by increasing the radii of these reflecting bodies. This setup, with reflecting bodies having a radius of 1.1, is illustrated in the inset of Figure 8. Given a particular radius, we define a confining number (ρ) by considering the octagon passing through the center of the reflecting bodies and define ρ to be the

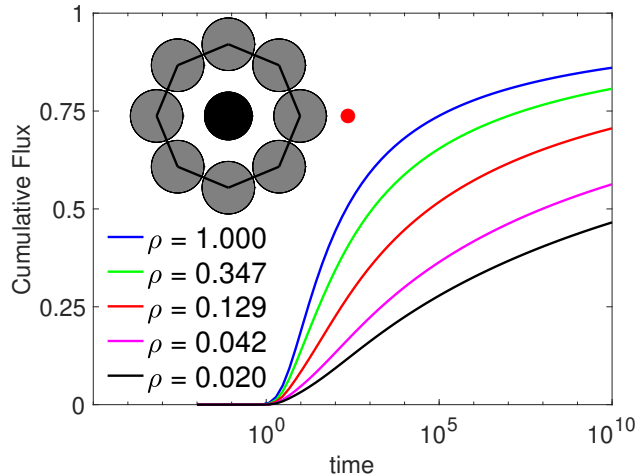


Figure 8: The cumulative flux into an absorbing trap (black circle) in the middle of eight reflecting bodies (gray bodies). The particles are initiated at the red dot. The confining ratio ρ is the ratio of the perimeter of the octagon (black curve) that is outside the reflecting bodies relative to the perimeter of the entire octagon. The confining ratio of the inset is $\rho = 0.129$.

ratio of the octagon’s perimeter that is outside of the reflecting bodies to the total perimeter of the octagon.

The cumulative flux into the absorbing body is shown in Figure 8. Each line corresponds to a different confining ratio ρ . The $\rho = 1$ curve corresponds to the scenario with no reflecting bodies, and the exact solution in Laplace space is given by equation (38). The case $\rho = 0$ corresponds to the vanishing gap limit in which the absorber is not accessible from the initial location. As expected, increasing the radii of the reflecting bodies (lowering ρ) decreases the cumulative flux at any particular time. In the most shielded example ($\rho = 0.020$), not even 50% of the cumulative flux of particles are absorbed at time $t = 10^{10}$. These distributions have so much weight in their tails that Monte Carlo methods are not appropriate for these examples.

A heat map of $p(\mathbf{x}, t)$ is shown in Figure 9 for each of the four non-zero radii of the reflecting bodies, and at three values of t . Because the Talbot contour scales with t^{-1} , the numerical solution at the earliest time has enough Talbot quadrature error that a halo appears around the support of the solution (left column). However, at later times, the numerical solution is very smooth (right column). At these three early times, the difference between the solutions is slight, in particular we see small differences in the density near the gap between reflectors. However, our method allows us to compute the solution at much later times, a calculation that would be very challenging using particle based Monte Carlo methods. In Figure 10, we plot the solution at time $t = 10^{10}$. At the highest level of shielding ($\rho = 0.020$), we see that a particle is about 100 times more likely to be found at a particular point outside the ring of reflecting bodies of the cage than at a point inside the ring of reflecting bodies.

4.5. Multiple Absorbing Traps and Escape from a Maze Geometry

The Faraday cage example involves multiple reflecting bodies, but only a single absorbing body. In this example, we consider escape from a *maze-like* geometry formed by rectangular blocks with reflecting boundary conditions. We consider a particle originating at the center of the maze which diffuses towards one of three exits. The likelihood of taking a particular exit from the maze is

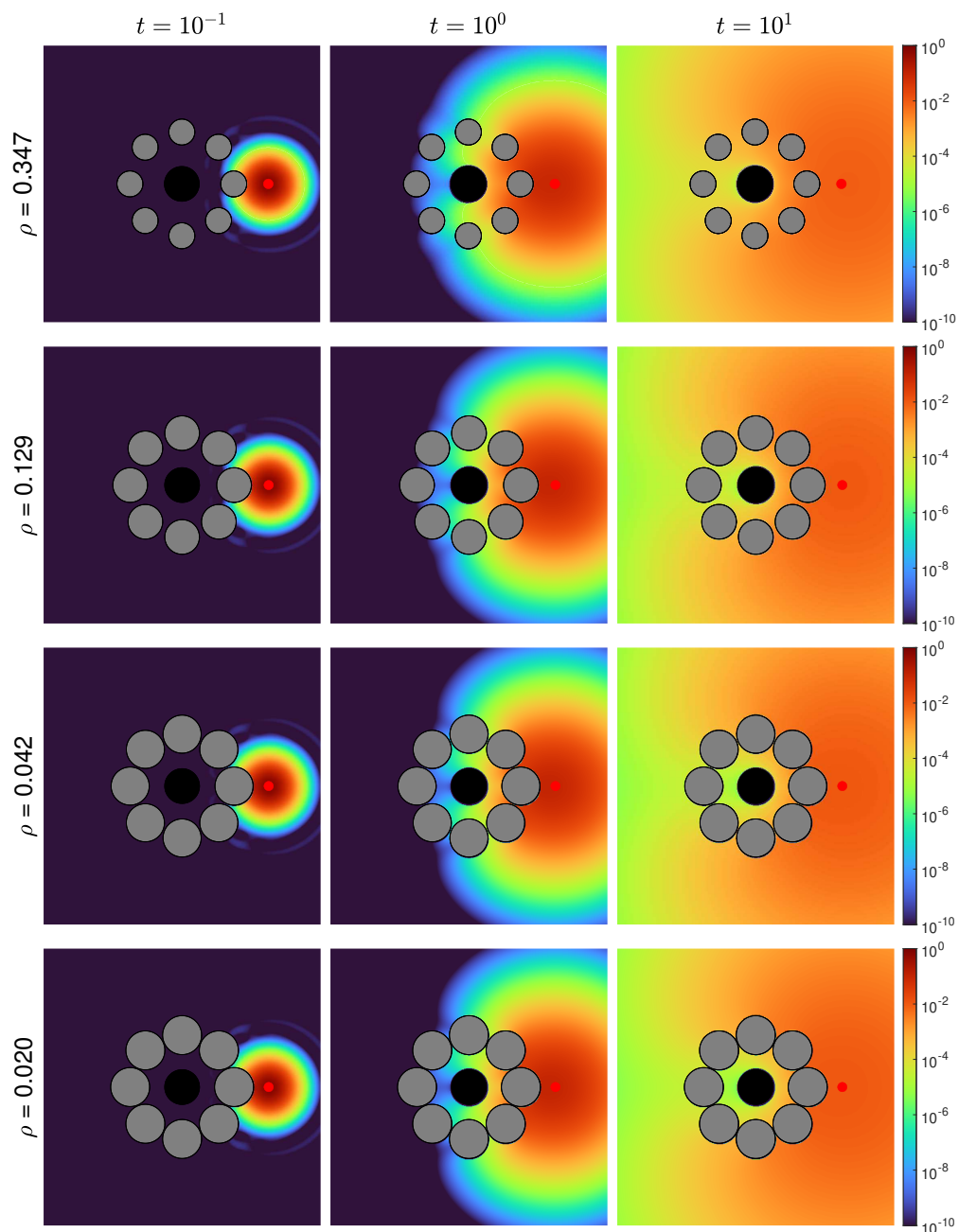


Figure 9: A heat map of solutions $p(\mathbf{x}, t)$ to (2) at short times $t = \{10^{-1}, 10^0, 10^1\}$. The gray circles are reflecting, the black circle is absorbing, and the particle is initialized at the red dot. From top to bottom, the geometries are defined by their confining ratios $\rho = \{0.347, 0.129, 0.042, 0.020\}$.

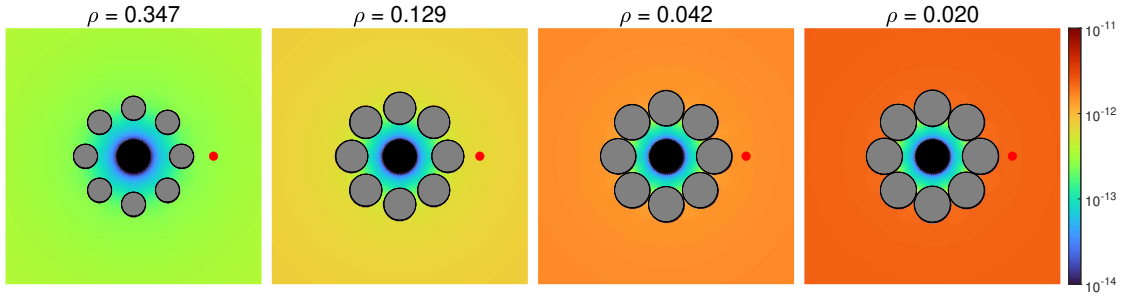


Figure 10: Heat maps of solutions $p(\mathbf{x}, t)$ to (2) at $t = 10^{10}$ for geometries with confining ratios $\rho = \{0.347, 0.129, 0.042, 0.020\}$. At the highest level of shielding ($\rho = 0.020$), we see that a particle is roughly 100 times more likely to be found at a particular point outside the ring of reflecting bodies of the cage than at a point inside the ring of reflecting bodies.

evaluated by calculating the cumulative flux at absorbing disks placed at each of these apertures. A schematic of the geometric setup is shown in the inset of Figure 11.

In the dynamic results shown in Figure 11, we see that for a diffusing particle initialized at the point shown, the blue exit is the most likely to absorb a particle with probability 45.8%, the green exit is the second most likely with probability 32.2%, and the red exit is the least likely with probability 22.0%. These quantities, which describe the likelihood of hitting any particular absorber, are known as the *splitting probabilities* and are important in ecological and signaling applications [32, 33, 40]. In this example, we observe a much faster equilibration timescale due to the fact that the geometry of the maze funnels most density close to one of the three absorbers. In terms of particle trajectories, this means that very few particles escape the maze and the absorbers while transitioning the exits. Heat maps of $p(\mathbf{x}, t)$ are shown in Figure 12.

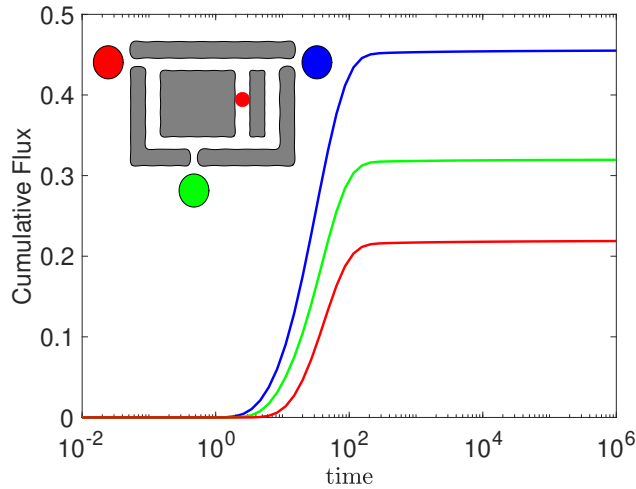


Figure 11: The cumulative flux into three absorbing traps (colored disks) surrounding a maze of reflecting bodies (gray bodies) with the initialization point at the center of the maze (red dot). The colors of the cumulative flux curves match those of the absorbing disks. Our numerical results show that a diffusing particle will most likely be absorbed by the blue exit, followed by the green exit, and is least likely to be absorbed by the red exit.

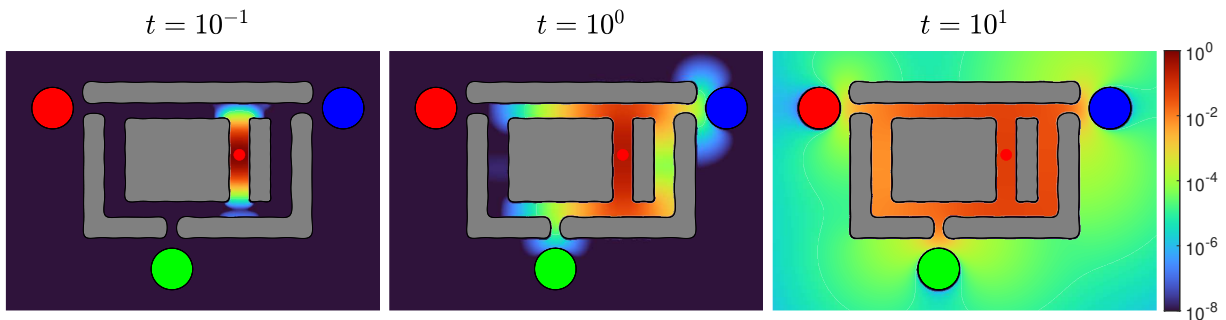


Figure 12: The heat map of solutions $p(\mathbf{x}, t)$ to (2) at three early times $t = \{10^{-1}, 10^0, 10^1\}$. The gray polygons are reflecting, the colored disks are absorbers denoting the maze exits, and the particle is initialized at the maze center (red dot).

5. Conclusions

We have introduced a method for the numerical solution of planar diffusion problems through a coupling of boundary integral methods with the Laplace transform. The main application of the approach is to determine the capture rate of diffusing particles to absorbing sites through complex geometries. In particular, the methods presented here can accommodate unbounded geometries comprised of entirely Dirichlet and entirely Neumann disjoint elements, a scenario that poses a particular challenge to particle-based methods which can become stuck on reflecting sections.

Future work should extend this approach to bodies with more general boundary conditions, including the Robin case and the scenario of a mixture of Neumann and Dirichlet. The scenario of mixed boundary conditions arises in cellular signaling where the role of receptors is modeled through the inclusion of numerous small Dirichlet windows in an otherwise reflecting body [3, 28, 33, 36]. The case of mixed conditions has been explored previously for the Helmholtz equation [17] and it would be natural to combine that approach with the Laplace transform approach of the present work to enable an extension to parabolic problems. The Robin boundary condition arises when replacing the mixed boundary conditions by an effective one of form

$$\frac{\partial p}{\partial \mathbf{n}} = \sigma p, \quad \mathbf{x} \in \Gamma_R. \quad (39)$$

The replacement of a mixture of Dirichlet and Neumann boundary conditions by a uniform Robin condition (39) is known as *boundary homogenization* [4, 45, 49]. This reduction is a great simplification and is accurate provided the permeability parameter σ is chosen in a way to mimic the capture rate of the bodies Γ .

Another important extension of the present work is to handle more general initial conditions. We remark that our method relies on a known particular solution of the transform equation to arrive a homogeneous problem which is solvable by boundary integral means. In the scenario where the initial condition is a point source, or a summation of point sources, this particular solution is representable as a combination of fundamental solutions. For extensions to more general initial conditions, this particular solution can be represented as a convolution, however, this introduces an area integral requiring careful evaluation. Extensions to moving geometries [37, 38, 60] and eroding geometries [13, 44, 51], which can be simulated with BIEs, are additional important directions for future studies.

Acknowledgments. A.E.L. acknowledges support under National Science Foundation award DMS 2052636. B.D.Q. acknowledges support under National Science Foundation award DMS 2012560.

References

- [1] Ludvig af Klinteberg, Travis Askham, and Mary Catherine Kropinski. A Fast Integral Equation Method for the Two-Dimensional Navier-Stokes Equations. *Journal of Computational Physics*, 409:109353, 2020.
- [2] B. K. Alpert. Hybrid Gauss-Trapezoidal Quadrature Rules. *SIAM Journal on Scientific Computing*, 20:1551–1584, 1999.
- [3] A. J. Bernoff and A. E. Lindsay. Numerical approximation of diffusive capture rates by planar and spherical surfaces with absorbing pores. *SIAM Journal on Applied Mathematics*, 78(1): 266–290, 2018.
- [4] A. J. Bernoff, A. E. Lindsay, and D. D. Schmidt. Boundary homogenization and capture time distributions of semipermeable membranes with periodic patterns of reactive sites. *SIAM Journal on Multiscale Modeling & Simulation*, 16(3):1411–1447, 2018.
- [5] Andrew J. Bernoff, Alexandra Jilkine, Adrián Navarro Hernández, and Alan E. Lindsay. Single-cell directional sensing from just a few receptor binding events. *Biophysical Journal*, 122(15): 3108–3116, 2023.
- [6] Paul C. Bressloff and Jay M. Newby. Stochastic models of intracellular transport. *Reviews of Modern Physics*, 85:135–196, Jan 2013. doi: 10.1103/RevModPhys.85.135. URL <https://link.aps.org/doi/10.1103/RevModPhys.85.135>.
- [7] S. L. Campbell, I. C. F. Ipsen, C. T. Kelley, C. D. Meyer, and Z. Q. Xue. Convergence estimates for solution of integral equations with GMRES. *Journal of Integral Equations and Applications*, 8(1):19–34, 1996.
- [8] Matthew Causley, Andrew Christlieb, Benjamin Ong, and Lee Van Groningen. Method of Lines Transpose: An Implicit Solution to the Wave Equation. *Mathematics of Computation*, 83(290):2763–2786, 2014.
- [9] Roman Chapko and Rainer Kress. Rothe’s Method for the Heat Equation and Boundary Integral Equations. *Journal of Integral Equations and Applications*, 9(1):47–69, 1997.
- [10] S. Jonathan Chapman, David P. Hewett, and Lloyd N. Trefethen. Mathematics of the Faraday Cage. *SIAM Review*, 57(3):398–417, 2015.
- [11] A.H-D. Cheng, Y. Abousleiman, and T. Badmus. A Laplace transform BEM for axisymmetric diffusion utilizing pre-tabulated Green’s function. *Engineering Analysis with Boundary Elements*, 9:39–46, 1992.
- [12] Jake Cherry, Alan E. Lindsay, Adrián Navarro Hernández, and Bryan Quaife. Trapping of Planar Brownian Motion, Full First Passage Time Distributions by Kinetic Monte-Carlo, Asymptotic and Boundary Integral Equations. *SIAM Journal on Multiscale Modelling and Simulation*, 20(4):1284–1314, 2022.

- [13] Shang-Huan Chiu, M. N. J. Moore, and Bryan Quaife. Viscous transport in eroding porous media. *Journal of Fluid Mechanics*, 893:A3, 2020.
- [14] Martin Costabel and Francisco-Javier Sayas. Time-dependent problems with the boundary integral equation method. *Encyclopedia of Computational Mechanics*, 1:703–721, 2004.
- [15] Benedict Dingfelder and J. A. C. Weideman. An improved talbot method for numerical laplace transform inversion. *Numerical Algorithms*, 68(1):167–183, 2015.
- [16] Fredrik Fryklund, Mary Catherine A. Kropinski, and Anna-Karin Tornberg. An integral equation based numerical method for the forced heat equation on complex domains. *Advances in Computational Mathematics*, 43:1–36, 2020.
- [17] Adrianna Gillman. An integral equation technique for scattering problems with mixed boundary conditions. *Advances in Computational Mathematics*, 43(2):351–364, 2017.
- [18] D. Grebenkov, R. Metzler, and G. Oshanin. *Target Search Problems*. Springer Nature Switzerland, 2024.
- [19] L. Greengard and J.-R. Li. On the numerical solution of the heat equation I: Fast solvers in free space. *Journal of Computational Physics*, 226:1891–1901, 2007.
- [20] L. Greengard and J. Strain. A Fast Algorithm for the Evaluation of Heat Potentials. *Communications on Pure and Applied Mathematics*, 43(8):949–963, 1990.
- [21] B.J. Gross, P. Kuberry, and P.J. Atzberger. First-passage time statistics on surfaces of general shape: Surface PDE solvers using Generalized Moving Least Squares (GMLS). *Journal of Computational Physics*, 453:110932, 2022. ISSN 0021-9991. doi: <https://doi.org/10.1016/j.jcp.2021.110932>. URL <https://www.sciencedirect.com/science/article/pii/S0021999121008275>.
- [22] Johan Helsing. *Solving integral equations on piecewise smooth boundaries using the RCIP method: a tutorial*, 2013.
- [23] George C. Hsiao and J. Saranen. Boundary Integral Solution of the Two-dimensional Heat Equation. *Mathematical Methods in the Applied Sciences*, 16:87–114, 1993.
- [24] Chi-Ok Hwang and Michael Mascagni. Electrical capacitance of the unit cube. *Journal of Applied Physics*, 95(7):3798–3802, 2004. doi: 10.1063/1.1664031. URL <https://doi.org/10.1063/1.1664031>.
- [25] Chi-Ok Hwang, Michael Mascagni, and Taeyoung Won. Monte Carlo methods for computing the capacitance of the unit cube. *Mathematics and Computers in Simulation*, 80(6):1089–1095, 2010.
- [26] Shidong Jiang, Leslie Greengard, and Shaobo Wang. Efficient sum-of-exponentials approximations for the heat kernel and their applications. *Advances in Computational Mathematics*, 41(3):529–551, 2015.
- [27] Sharad Kapur and Vladimir Rokhlin. High-Order Corrected Trapezoidal Quadrature Rules for Singular Functions. *SIAM Journal on Numerical Analysis*, 34(4):1331–1356, 1997.

- [28] Jason Kaye and Leslie Greengard. A fast solver for the narrow capture and narrow escape problems in the sphere. *Journal of Computational Physics: X*, 5:100047, 2020.
- [29] Rainer Kress. *Linear Integral Equations*. Applied Mathematical Sciences. Springer, 1999.
- [30] M.C. Kropinski and B.D. Quaife. Fast integral equation methods for Rothe’s method applied to the isotropic heat equation. *Computers and Mathematics with Applications*, 61:2436–2446, 2010.
- [31] M.C. Kropinski and B.D. Quaife. Fast integral equation methods for the modified Helmholtz equation. *Journal of Computational Physics*, 230:425–434, 2011.
- [32] V. Kurella, JC. Tzou, D. Coombs, and MJ. Ward. Asymptotic Analysis of First Passage Time Problems Inspired by Ecology. *Bulletin of Mathematical Biology*, 77(1):83–125, 2015.
- [33] Sean D Lawley, Alan E Lindsay, and Christopher E Miles. Receptor Organization Determines the Limits of Single-Cell Source Location Detection. *Physical Review Letters*, 125(1):018102, Jul 2020.
- [34] Jing-Rebecca Li and Leslie Greengard. High order accurate methods for the evaluation of layer heat potentials. *SIAM Journal on Scientific Computing*, 31(5):3847–3860, 2009.
- [35] A. E. Lindsay, R.T. Spoonmore, and J.C. Tzou. Hybrid asymptotic-numerical approach for estimating first passage time densities of the two- dimensional narrow capture problem. *Physical Review E*, 94:042418, 2016.
- [36] A. E. Lindsay, A. J. Bernoff, and M. J. Ward. First Passage Statistics for the Capture of a Brownian Particle by a Structured Spherical Target with Multiple Surface Traps. *SIAM Journal on Multiscale Modeling and Simulation*, 15(1):74–109, 2017.
- [37] A. E. Lindsay, J. C. Tzou, and T. Kolokolnikov. Optimization of First Passage Times by Multiple Cooperating Mobile Traps. *SIAM Journal on Multiscale Modeling & Simulation*, 15(2):920–947, 2017. doi: 10.1137/16M1060169.
- [38] AE. Lindsay, T. Kolokolnikov, and JC. Tzou. Narrow escape problem with a mixed trap and the effect of orientation. *Physical Review E*, 91:032111, 2015. doi: 10.1103/PhysRevE.91.032111. URL <https://link.aps.org/doi/10.1103/PhysRevE.91.032111>.
- [39] Alan E. Lindsay and Andrew J. Bernoff. Kinetic Monte Carlo methods for three-dimensional diffusive capture problems in exterior domains. *arxiv*, 2406.13644, 2024. URL <https://arxiv.org/abs/2406.13644>.
- [40] Alan E. Lindsay, Andrew J. Bernoff, and Adrián Navarro Hernández. Short-time diffusive fluxes over membrane receptors yields the direction of a signalling source. *Royal Society Open Science*, 10(4):221619, 2023.
- [41] Jingwei Ma, Myan Do, Mark A. Le Gros, Charles S. Peskin, Carolyn A. Larabell, Yoichiro Mori, and Samuel A. Isaacson. Strong intracellular signal inactivation produces sharper and more robust signaling from cell membrane to nucleus. *PLOS Computational Biology*, 16(11):1–19, 11 2020. doi: 10.1371/journal.pcbi.1008356. URL <https://doi.org/10.1371/journal.pcbi.1008356>.

- [42] Ava J. Mauro, Jon Karl Sigurdsson, Justin Shrake, Paul J. Atzberger, and Samuel A. Isaacson. A First-Passage Kinetic Monte Carlo method for reaction–drift–diffusion processes. *Journal of Computational Physics*, 259:536–567, 2014. ISSN 0021-9991. doi: <https://doi.org/10.1016/j.jcp.2013.12.023>. URL <https://www.sciencedirect.com/science/article/pii/S002199911300822X>.
- [43] Yu. A. Melnikov and V. Reshniak. A semi-analytical approach to Green’s functions for heat equation in regions of irregular shape. *Engineering Analysis with Boundary Elements*, 46:108–115, 2014.
- [44] Nicholas J. Moore, Jake Cherry, Shang-Huan Chiu, and Bryan D. Quaipe. How fluid-mechanical erosion creates anisotropic porous media. *Physica D*, 445:133634, 2023.
- [45] C. B. Muratov and S. Y. Shvartsman. Boundary homogenization for periodic array of absorbers. *SIAM Journal on Multiscale Modeling and Simulation*, 7(1):44–61, 2008.
- [46] Kyriacos Nicolaou and Bela M. Mulder. A probabilistic algorithm for optimising the steady-state diffusional flux into a partially absorbing body. *Scientific Reports*, 13:22815, 2023.
- [47] Monika Nitsche. Evaluation of near-singular integrals with application to vortex sheet flow. *Theoretical and Computational Fluid Dynamics*, 35:581–608, 2021.
- [48] Scott H. Northrup. Diffusion-controlled ligand binding to multiple competing cell-bound receptors. *The Journal of Physical Chemistry*, 92(20):5847–5850, 1988. doi: 10.1021/j100331a060. URL <http://dx.doi.org/10.1021/j100331a060>.
- [49] Claire E. Plunkett and Sean D. Lawley. Boundary Homogenization for Partially Reactive Patches. *SIAM Journal on Multiscale Modeling & Simulation*, 22(2):784–810, 2024. doi: 10.1137/23M1573422.
- [50] Tianyu Qiu, Alexander Rieder, Francisco–Javier Sayas S, and Shougui Zhang. Time-domain boundary integral equation modeling of heat transmission problems. *Numerische Mathematik*, 143:223–259, 2019.
- [51] Bryan Quaipe and M. Nicholas J. Moore. A boundary-integral framework to simulate viscous erosion of a porous medium. *Journal of Computational Physics*, 375:1–21, 2018.
- [52] Ryan D. Schumm and Paul C. Bressloff. A numerical method for solving snapping out Brownian motion in 2D bounded domains. *Journal of Computational Physics*, 493:112479, 2023.
- [53] Avram Sidi and Moshe Israeli. Quadrature Methods for Periodic Singular and Weakly Singular Fredholm Integral Equations. *Journal of Scientific Computing*, 3(2):201–231, 1988.
- [54] J. Sladek, V. Sladek, and Ch. Zhang. Transient heat conduction analysis in functionally graded materials by the meshless local boundary integral equation method. *Computational Materials Science*, 28(3):494–504, 2003.
- [55] Tracy L. Stepien, Cole Zmurchok, James B. Hengenius, Rocío Marilyn Caja Rivera, Maria R. D’Orsogna, and Alan E. Lindsay. Moth Mating: Modeling Female Pheromone Calling and Male Navigational Strategies to Optimize Reproductive Success. *Applied Sciences*, 10:6543, 2020.

- [56] John Strain. Fast Adaptive Methods for the Free-Space Heat Equation. *SIAM Journal on Scientific Computing*, 15(1):185–206, 1994.
- [57] Alok Sutradhar, Glaucio H. Paulino, and L.J. Gray. Transient heat conduction in homogeneous and non-homogeneous materials by the Laplace transform Galerkin boundary element method. *Engineering Analysis with Boundary Elements*, 26:119–132, 2002.
- [58] Johannes Tausch. A fast method for solving the heat equation by layer potentials. *Journal of Computational Physics*, 224:956–969, 2007.
- [59] Lloyd N. Trefethen and J. A. C. Weideman. The Exponentially Convergent Trapezoidal Rule. *SIAM Review*, 56(3):385–458, 2014.
- [60] J. C. Tzou and T. Kolokolnikov. Mean First Passage Time for a Small Rotating Trap inside a Reflective Disk. *SIAM Journal on Multiscale Modeling & Simulation*, 13(1):231–255, 2015. doi: 10.1137/140968604.
- [61] S.K. Veeranpaneni and G. Biros. A High-Order Solver for the Heat Equation in 1D domains with Moving Boundaries. *SIAM Journal on Scientific Computing*, 29, 2006.
- [62] Shravan K. Veerapaneni and George Biros. The Chebyshev fast Gauss and nonuniform fast Fourier transforms and their application to the evaluation of distributed heat potentials. *Journal of Computational Physics*, 227:7768–7790, 2008.
- [63] Jun Wang and Leslie Greengard. An Adaptive Fast Gauss Transform in Two Dimensions. *SIAM Journal on Scientific Computing*, 40(3):A1274–A1300, 2018.